Dynamic Stall and its Passive Control Investigations on the OA209 Airfoil Section

by
Wolfgang Geissler, Guido Dietz, Holger Mai,
Johannes Bosbach, Hugues Richard, DLR-Göttingen,Germany

Abstract:

Within the joint DLR/ONERA project "Dynamic Stall" it was decided to select the ONERA OA209 airfoil section as a candidate for common comprehensive numerical as well as experimental investigations. While at ONERA the low speed aspects have mainly been addressed and experiments have been carried out in the F2-wind-tunnel facility in Fougat, France, DLR has concentrated on investigations in the compressible flow regime starting at Ma=0.3 and reaching into the transonic flow regime up to Ma=0.75.
In the present paper recent experimental investigations are presented which have been conducted in the 1mx1m transonic wind-tunnel facility DNW-TWG located at DLR-Göttingen in a two weeks test-campaign during October/November 2004. The tests have been done in a joint effort between the DLR Institute of Aerodynamics and Flow Technology (AS) and the DLR Institute of Aeroelasticity (AE) both located at the DLR site in Göttingen, Germany.
Two main topics have been addressed during the test campaign:

1) Steady, Light- and Deep Dynamic Stall investigations on the clean blade section,
2) Exploratory studies of passive control during dynamic stall by means of miniature **L**eading **E**dge **VO**rtex **G**enerators, (LEVOGs).

The blade model with 0.3m chord and 1m span (arranged between wind-tunnel side walls) was equipped with 45 pressure sensors (Kulites) along the mid-span section of the model. In addition to unsteady pressure measurements PIV recordings have been taken for each test point.
Corresponding numerical calculations for the clean airfoil have been done on the basis of a 2D-time accurate Navier-Stokes code for comparisons with the experimental data.

1. Introduction.

The joint project "Dynamic Stall" as arranged between DLR and ONERA started in 2001 and will end in 2005 with the option to be extended over a further period. Main emphasis within this project has been placed on numerical as well as experimental investigations of the physical phenomenon "Dynamic Stall". Although numerous investigations have been carried out recently, i.e. [1],[2] this phenomenon still remains with a number of unknowns. The role of compressibility has been studied in [3] but it is not clear yet how a local small supersonic bubble triggers the onset of dynamic stall. Transition on the oscillating blade is another candidate to be investigated carefully, [4]. The time dependent development of transition during dynamic stall and its role to initiate dynamic stall is also still not resolved in detail. Measurements in this respect are of high interest in order to get information how to improve transition modelling in numerical codes. Further the combination of both transition and compressibility has a strong impact on the flow development at very specific input parameters (Mach, incidence combination).
Further DLR has started a new main topic inside the joint project with Dynamic Stall **control** activities. A comprehensive study of the dynamic **nose-droop concept** has been presented in [5], [6] as a joint effort between DLR, Eurocopter Deutschland (ECD) and EADS-company. Similar investigations have been carried out recently in a joint effort between DLR and US-Army in Ames Research Centre within the scope of a Memorandum of Understanding (MoU), [7].
These dynamic stall control activities have been very effective and have shown a considerable potential of the nose-drooping device. The work is ongoing and a decision is sought how to continue the next couple of years.
However the nose-drooping concept has also been criticized: The effort to implement a moving leading edge flap over part of the blade span is a formidable task on a real helicopter rotor. Fail proof and sufficiently strong actuators have to be developed to operate the flap in a position where the aerodynamic loading is extremely high and where the flow is changing rapidly during the dynamic stall cycle.
Therefore the present study has started to follow a different philosophy, i.e. the development of **passive** dynamic stall control devices. Here different possibilities exist as well and have also already been addressed in literature, i.e. [8]. Due to the experience of a number of comprehensive investigations in DLR, [9],[10],[11] the flow details during dynamic stall have been studied by both experimental as well as numerical tools. From this knowledge base it is now possible to implement devices, i.e. miniature vortex generators at positions, where these devices are most efficient.

In the present paper the experimental data measured with unsteady pressure sensors as well as with the PIV-technique will first be analyzed for the clean wing (no vortex generators) and compared in detail with numerical data.
In a second step **L**eading **E**dge **VO**rtex **G**enerators (LEVOGs) will be added and their effect on dynamic stall will be studied. In these flow cases a local 3D-flow is developing along the 2D-blade model. Corresponding numerical data have not been calculated at the moment because a suitable 3D-numerical code has to be used for this purpose. In the future the DLR-TAU-code will be utilized for this task.

2. Model and Test Facility.

The blade section model has been designed and constructed in the DLR-workshop in Braunschweig. The model is made from composite material to minimize weight and maximize stiffness. The airfoil used for the blade section is the OA209 airfoil as decided to be the standard airfoil of the DLR/ONERA project "Dynamic Stall". The model chord is 0.3m, the model span is 1m to fit between the tunnel side walls.
The test site is the DNW-TWG wind-tunnel located at the DLR-site Göttingen, Germany. This tunnel has a 1mx1m test section with adaptive upper and lower wind-tunnel walls.

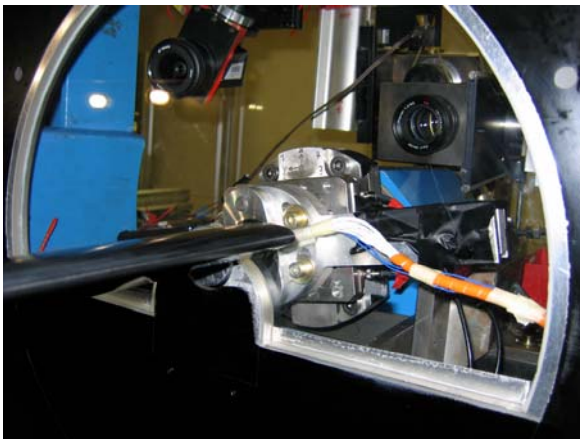

Fig.1: Model and model suspension in TWG-Test Section

Fig.1 and 2 show the model with its suspension in the wind-tunnel test section as well as outside the test section. The model is oscillated about its quarter chord axis by means of hydraulic actuators (see Fig.2) operated by the DLR Institute AE. The arrangement seen in Figs. 1 and 2 is doubled on the opposite side of the tunnel test section to definitely avoid model distortion. The model is equipped with a total of 45 miniature pressure sensors (Kulites) along the model mid-span. Two accelerometers have been installed to control model distortion. Data acquisition and reduction has also been done

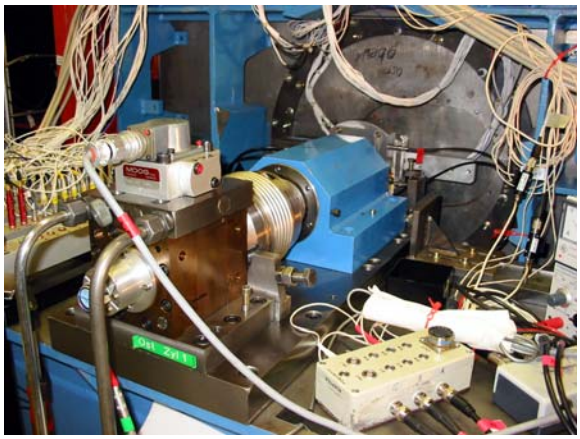

Fig.2: Hydraulic actuator, bearing of model suspension

by the Institute AE using their common data evaluation procedure (AMIS II).
In Fig.1 two cameras are visible which belong to the PIV-measurement system of the Institute AS.
This system will be described in detail in section 4.

3. Numerical Code.

As in recent investigations ([4] and [9]-[11]) a time accurate Navier-Stokes code (URANS) for 2D-flows has been used to calculate the unsteady air loads about oscillating airfoils.
This code has been described in [12]. The numerical solution procedure is based on the Approximate Factorization Implicit methodology originally developed by Beam and Warming, [13]. The code represents the full NS-equations and is working on structured grids in a space fixed frame of reference. With this arrangement the grid is allowed to deform during oscillation – a pre-requisite to handle dynamic airfoil deformations as realized in ref. [9]-[11].
The code is also equipped with various turbulence models reaching from the algebraic Baldwin-Lomax via the one-equation Spalart-Allmaras to the two equations k-ω-SST-model. In the present investigations the Spalart-Allmaras Model (SA) has been used throughout, [14]. As will be discussed later it is of considerable importance to take into account laminar-turbulent boundary-layer transition during the dynamic stall process. In [15] a transition model is described following Chen and Tyson's proposal for an exponential varying transition zone, [16] combined with Michel's criterion, [17] to determine transition onset. In this model the details of boundary-layer flow have first to be determined from the Navier-Stokes solution procedure. With this information dynamic stall onset is calculated following the procedure of Michel, [17] in a quasi-steady mode. The numerical results show a phase shift of stall onset to lower incidences if transition is taken into account. The fit to experimental data without boundary layer tripping is considerably improved.

4. PIV-Measurements.

Fig.1 shows the location of the two PCO-cameras looking through the observation window of the tunnel side-wall. **Fig.3** shows a sketch of the camera-views, airfoil and light sheet arrangements: To cover a larger area on the airfoil upper surface with a sufficient spatial resolution two cameras have been used in combination. With this arrangement almost 75% of the airfoil upper surface could be reached.
Camera 1 of the PCO-cameras was equipped with a 50mm lens and camera 2 was equipped with a 60mm lens respectively.

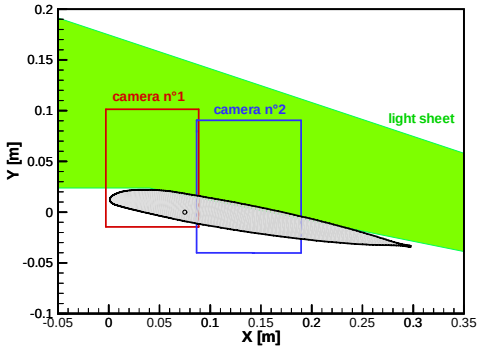

Fig.3: Sketch of PIV set-up

The laser light sheet, located along the model mid-span (in coincidence with the location of the pressure sensors) has been created by a Nd: Yag laser with 320 mJ per pulse. The seeding particles used in the tests are from DEHS with 1µm mean diameter.

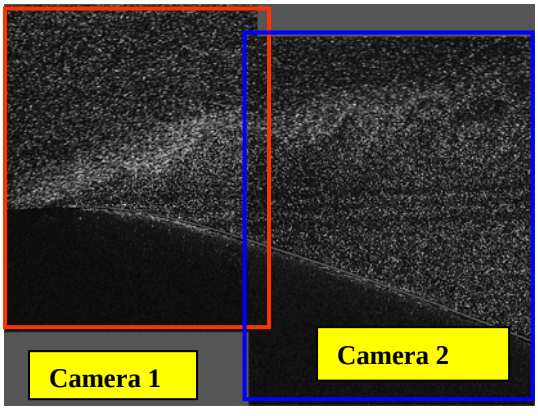

Fig.4: Example of PIV recording

Fig.4 shows an example of PIV recordings for a high instantaneous incidence of the blade during dynamic stall. From these recordings the corresponding velocity distributions and finally vorticity distributions have been evaluated. For the latter it must be kept in mind that a numerical differentiation has to be done from measured velocity fields. A scatter of the vorticity data is therefore not to be avoided (see PIV results).

For each single test point where unsteady pressures have been measured also PIV recordings were taken.
To compare both pressure and field data distributions one has to keep in mind that in the present test pressure-signals of the 45 Kulites have been taken for as much as 160 oscillatory cycles of the blade motion with 128 samples/cycle. Depending on the frequency of model oscillation only few PIV recordings per cycle could be measured. Finally a complete representative cycle of 16 PIV-recordings could only be received taking samples from different cycles of the motion. The present laser with a 10Hz pulse frequency could not resolve better in the time domain. However, the PIV recordings were taken synchronized with the Kulite data acquisition such that each PIV record corresponds to one instantaneous Kulite sample.

5. Results, Clean Wing

First of all results will be shown for the clean wing configuration without passive control devices be installed.
Beside steady polars unsteady hysteresis loops of lift-, drag- and pitching moment will be presented for both deep and light dynamic-stall cases. Then measured (PIV) and calculated vorticity fields will be compared for a deep dynamic stall case.

5.1 Steady Polars

Fig.5 shows a steady lift- and drag polar for M=0.31 and Re=1.15x10^6**.**

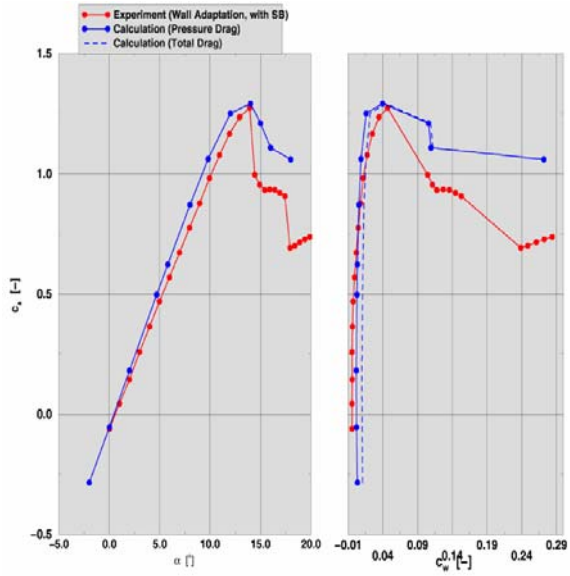

Fig.5: Steady lift- and drag polar, M=0.31, Re=1.15x10^6

The figure displays both numerical (blue) and experimental (red) data for comparison. A slight difference in lift slope is observed in the lift polar whereas the c_{lmax} values are in good coincidence. Concerning the drag variations (right plot) two

numerical results are included: calculation of the total drag (including friction drag, dashed blue line) and pressure drag alone (full blue line). The latter does compare much closer to the experimental data which also represents pressure drag alone as integrated from the pressure sensors. In the present case the Spalart-Allmaras one-equation turbulence model, [14] has been used in the calculations. Free transition has also been assumed in the numerical code.
For each of the measured incidences the wind-tunnel wall adaptation procedure of the DNW-TWG has been applied. So it is expected that wall interference effects in the present case are minimized. The calculations always assume free flight conditions.

5.2 Unsteady Force and Moment Hysteresis Loops.

In this section some few experimental data from the very large body of test results will be discussed in detail and compared with numerical calculations. First of all hysteresis loops of lift-, drag- and pitching moment will be compared for both deep and light stall conditions. Then some detailed pressure distributions in both time and space domain will be analysed. Corresponding PIV vorticity data will also be compared with calculations and a discussion of the various results will follow after each section.

- Deep Dynamic Stall

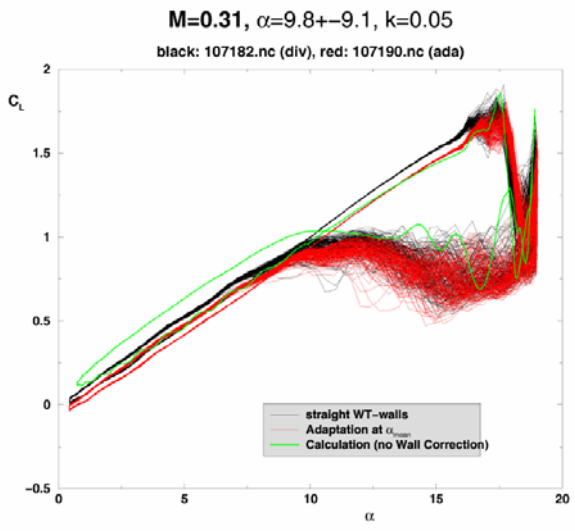

Fig.6a: Lift hystersis loops, α=9.8+/-9.1°, M=0.31, Re=1.15x10^6, k=0.05.

Figs 6a-c display lift-, drag- and pitching moment hysteresis loops for a deep dynamic-stall case at M=0.31 and k=0.05 reduced frequency (referred to half-chord). The plots include:

1) A set of experimental data from all 160 recorded cycles with straight wind-tunnel walls (black curves).

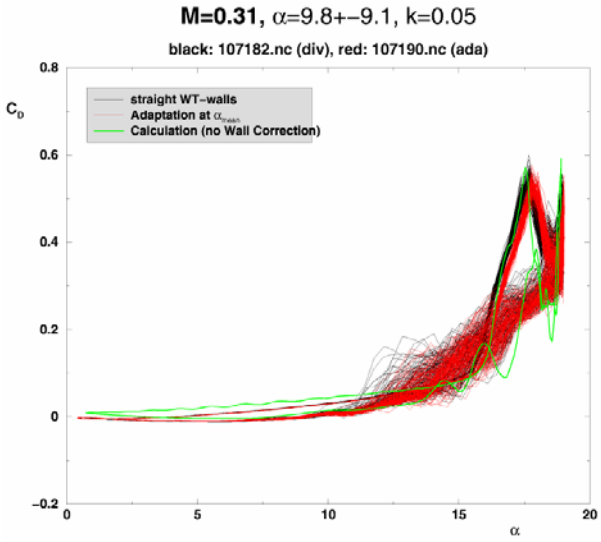

Fig.6b: Drag hystersis loops, α=9.8+/-9.1°, M=0.31, Re=1.15x10^6, k=0.05.

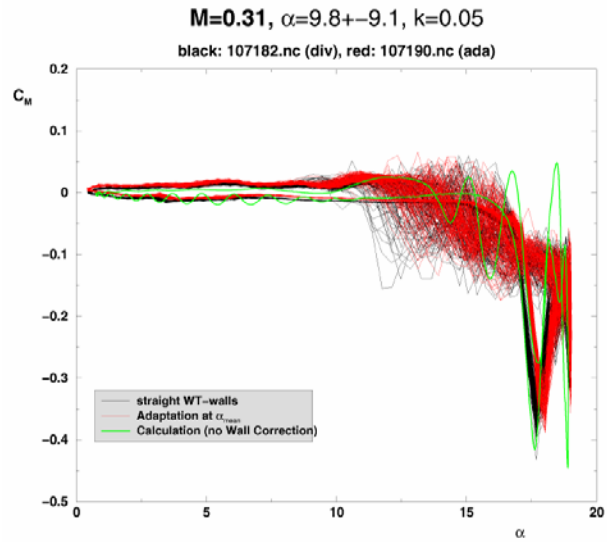

Fig.6c: Moment hystersis loops, α=9.8+/-9.1°, M=0.31, Re=1.15x10^6, k=0.05.

2) A set of experimental data from all 160 recorded cycles with wind-tunnel wall adaptation at the mean incidence (α=9.8°, red curves).
3) Numerical calculation, utilizing SA-turbulence model and free transition model (green curve).

A number of important effects can be detected from these plots.

Wind-Tunnel Wall Interference:
Concentrating on the experimental results first one can detect the effects of wind-tunnel walls on the force- and moment loops (differences between the black and red curves). For the lift the up-stroke part is shifted almost parallel to lower lift values per incidence. Only slight differences are found in the drag- and moment loops. Wind-tunnel wall adaptation as applied in the present case means, that

static wall adaptation is applied at the mean incidence of the cycle (i.e. at α=9.8^o). This wall contour is then kept fixed for the complete unsteady measurement. The numerical calculations are carried out with the assumption of free-flight condition. These conditions are simulated only at one single incidence in the experiment due to wall adaptation. Comparing the calculated lift curve with the adapted experiment (red curve) a best fit is achieved at several degrees higher as the mean incidence say at α=13^o. The reason is obvious: Due to the dynamics of the flow the best fit of static adaptation is shifted to a higher incidence in the unsteady case. Larger deviations between calculation and adapted experiment occur however at the minimum incidence where the static adaptation is inappropriate. It is very remarkable that these details can clearly be detected from calculations.

Spreading of Experimental Curves:

Another effect of the measured curves is the wide range spreading from cycle to cycle over parts of the loop. During up-stroke all 160 curves (see Fig.6a in particular) are on top of each other, the flow is non-separated in this range. Close to the maximum lift the curves begin to diverge as soon as the dynamic stall vortex with the beginning of separation on the upper surface is starting to move. The spreading of curves is continuing during the upper part of up-stroke where a severe drop of lift is observed in correspondence with drag- and negative pitching moment peaks. During down-stroke the spreading even exceeds until during the lower part of down-stroke all curves finally merge again into a single line.

Numerical Results:

The numerical results in Figs.6a-c (green curves) are of course represented by always a single line which is cyclic converged after about two complete calculated cycles. A remarkable coincidence exists between calculation and experiment concerning the up-stroke region up to dynamic stall onset but also at severe stall conditions where a secondary peak is observed in the experimental data and also in the calculation. In the latter case the effects of the secondary peak are slightly exaggerated (see Fig.6c, moment loops).

Only one single curve is shown if experimental data of dynamic-stall cases are discussed in the literature. This curve represents the phase locked average of all cycles displayed in Figs. 6. These results are indicated in **Fig.7**. In addition the curves representing the maximum and minimum margins of all curves are also included in these plots. In addition the numerical curves of Figs.6 have been added as well. If one compares the results of Fig.7 and Figs.6 one observes some important differences: For instance the peak values in lift are clearly reduced for the average experimental curve.

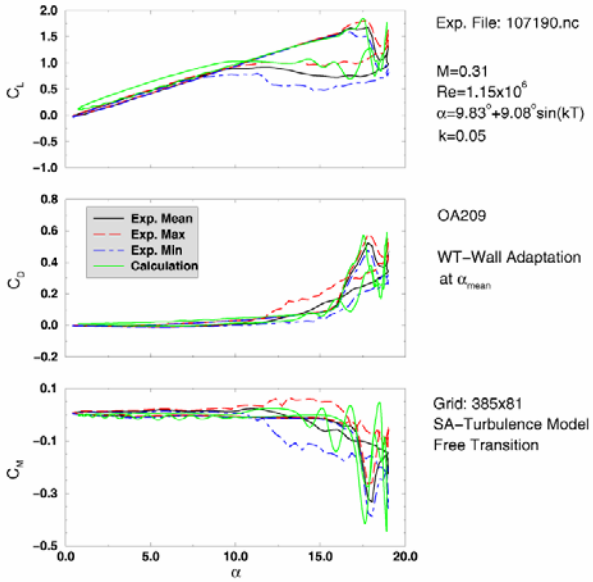

Fig.7: Measured force and moment loops as mean, maximum and minimum curves, comparison with calculation; Deep dynamic stall.

A larger deviation from calculation is suggested. Similar effects can be detected for the peaks in drag and moment as well as in the secondary peaks.

From these observations it can be deduced that it is of high importance to always look at the whole story, investigate all measured details and compare these with the calculations.

The present NS-Code calculates unsteady flows including separation, but the results do emerge to only one single curve. This behaviour is obvious: The calculation uses turbulence modelling which leads to an averaging of turbulence effects. In the experiment the turbulent outer flow influences the very sensitive separation regions and results in strong scatter from cycle to cycle as the turbulence field of the outer flow is changing.

The simulation of these effects is a formidable task: The turbulence details of the outer flow must be known and taken into account in the calculation process. This can only be done in DNS-(Direct Numerical Simulation) procedures where the information of the turbulent activities are measured in addition for all cycles. This scenario is not within the scope of the present investigations. On the other hand the correspondence between experiment and calculation as shown above is already sufficient and almost mature to serve as the basis for rotor blade design.

- Light Dynamic Stall

Figs. 8 show light dynamic-stall results similar to Fig.6. Now the best fit between experiment with wall adaptation and calculation is not so obvious. The best fit may be shifted again to about α=14^o where already separation is starting.

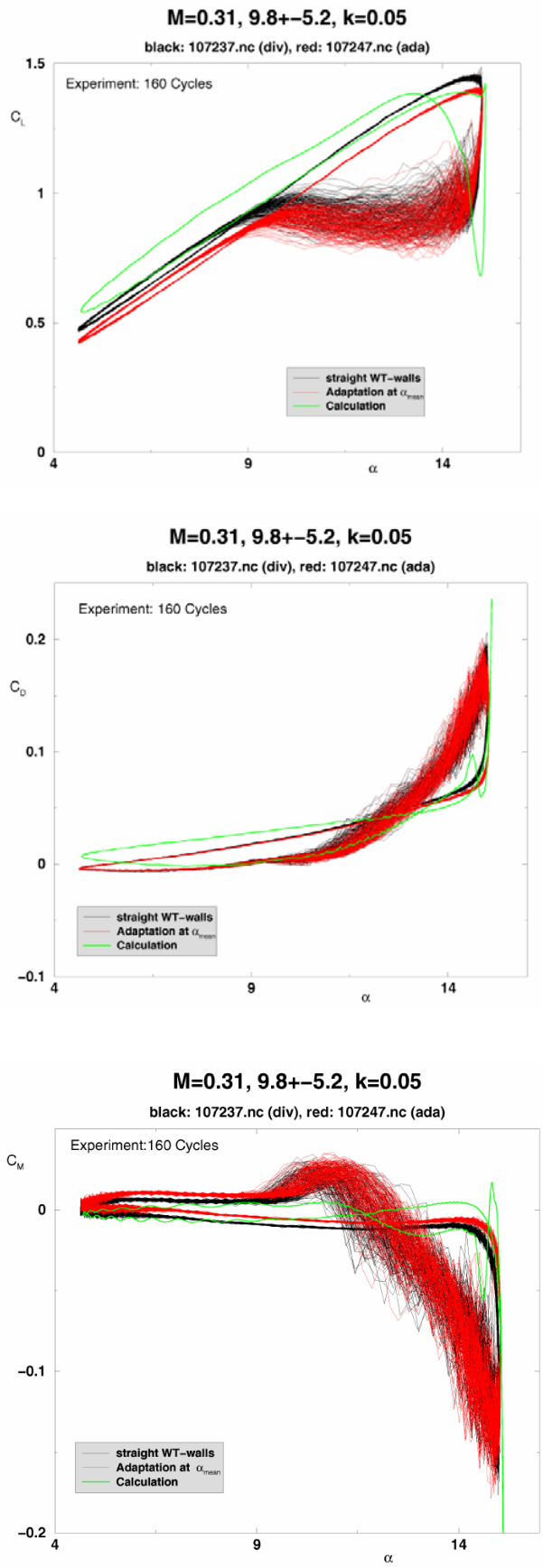

Fig.8: Lift- (upper), drag- (middle) and moment (lower) hysteresis loops for light dynamic stall: α=9.8+/-5.2°, M=0.31, Re=1.15x10^6, k=0.05

A negative peak in lift also found in drag and moment peaks is considerable exaggerated in the calculation. The reattachment process is calculated much earlier compared to the measured data.
Fig. 9 displays again the phase locked averages and margins of the experimental data including the numerical curves of Fig.8.

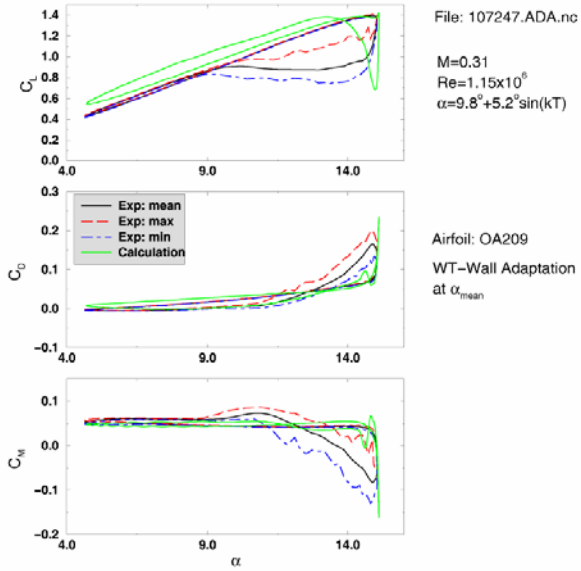

Fig.9: Measured force and moment loops as mean, maximum and minimum curves, comparison with calculation; Light dynamic stall.

Although not so obvious as in the deep dynamic stall case of Fig.7 the experimental mean-, maximum- and minimum-curves show some smoothing effects suggesting larger deviations in comparison to calculations.

5.3 Unsteady Pressures

For the deep dynamic stall case of Figs.6 and 7 some detailed unsteady pressure distributions will be investigated and compared with the corresponding numerical data. Two different ways to display pressure data have been chosen:

1) Pressure hysteresis loops similar to the force- and moment loops presented above at some selected chord-wise positions (upper surface)
2) Chord-wise pressure distributions at selected incidences; Incidence region at and beyond dynamic stall onset.

The displays of **Figs.10** include again all 160 consecutive measured cycles of the blade motion as well as the corresponding numerical data. At the airfoil leading edge (Fig.10, upper) the pressure peak due to the development of the dynamic stall vortex is very large and compares well with the calculation. Also a slightly exaggerated secondary pressure peak is following until during down-stroke

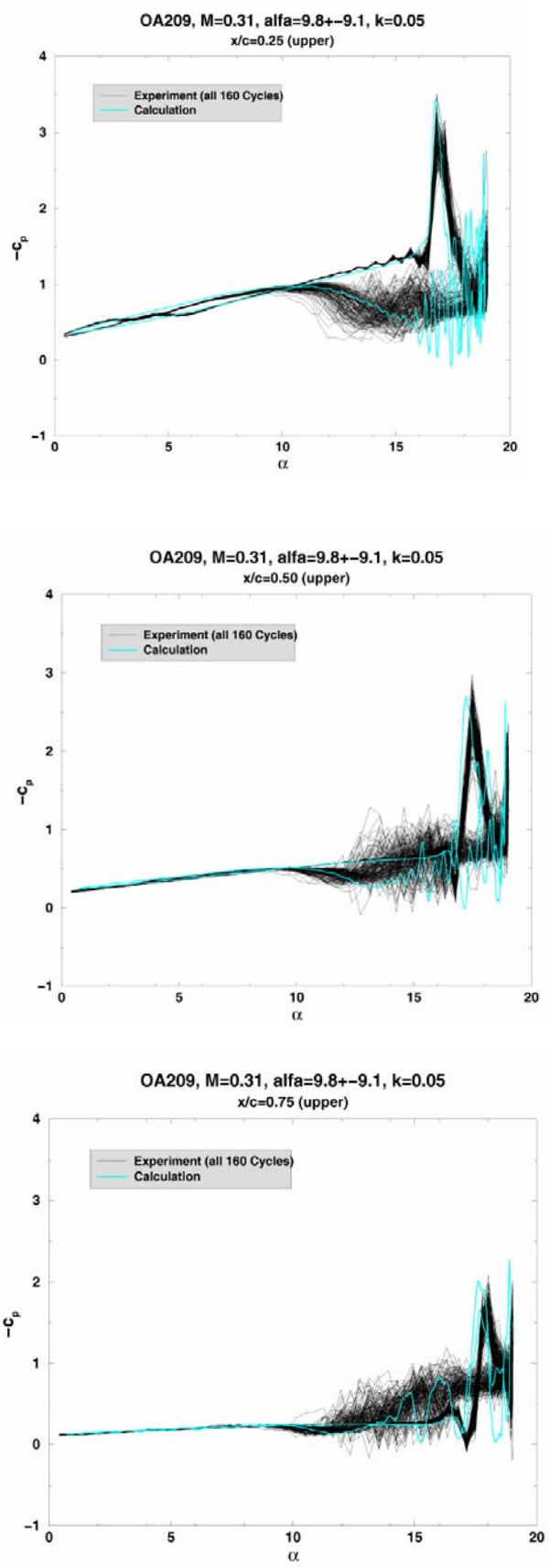

Fig.10: Pressure hysteresis loops at three selected chord-wise positions on upper surface: x/c=0.25 (upper), x/c=0.50 (middle), x/c=0.75 (lower); Deep dynamic stall.

some oscillations start which are dying out during the lower part of the down-stroke. These features are similar further down stream at x/c=0.50 and x/c=0.75.

Again the correspondence between measured and calculated data is surprisingly good. Oscillations occurring during the first phase of the down stroke are accompanied by similar excursions of the experimental curves. Further down stream the high frequencies of these oscillations are dying out in the calculation. The experimental curves show a similar behaviour over all chord-wise positions.

The secondary pressure peak is found in all three chord-wise positions. Its amplitudes are larger than the measured ones. The reason may be due to the fact that a secondary vortex does not behave as a 2D-vortex as the primary dynamic stall vortex does, but shows a more complex 3D topology due to the unsteady and separated flow environment in this part of the cycle. The calculation is 2D per se and assumes an ideal 2D structure also for the secondary vortex. The influence of this calculated secondary vortex is then stronger as in the experiment showing the exaggerated peaks discussed before also for the force- and moment distributions.

The second interesting way to display pressures is shown in **Fig.11**:

In this plot chord-wise pressure distributions are shown for different selected incidences during the deep dynamic stall case of Figs.6 and 7. For the experimental data a phase-locked average of all measured 160 cycles has been taken. The selection of incidences is such that dynamic-stall onset and the time instants beyond onset are investigated.

To make the interpretation of the results easier, experimental results are plotted as dots and calculations are displayed by solid curves in the same colour.

At $\alpha=15.6^o$ up-stroke the flow is definitely attached which is shown both by experiment (black dots) and calculation (black solid curve). Very short time later ($\alpha=15.99^o$) the experimental data (red dots) show the beginning of separation close to the leading edge, the calculation (red solid line) shows still attached flow. At $\alpha=16.38^o$ both calculated and measured pressure peaks at the leading edge break down forming an extra peak which is caused by the effect of the dynamic stall vortex. This vortex is now starting to move over the airfoil upper surface which can be detected from the moving pressure maximum expressed both in the numerical and experimental data.

As indicated in Fig.11 the computation now leads the experiment by about 10% chord length although the start of separation has taken place in the experiment prior to calculation. The travelling of the dynamic-stall vortex can be followed until the vortex lifts off the airfoil surface (widening of the pressure maximum) and finally leaves the airfoil from the trailing edge.

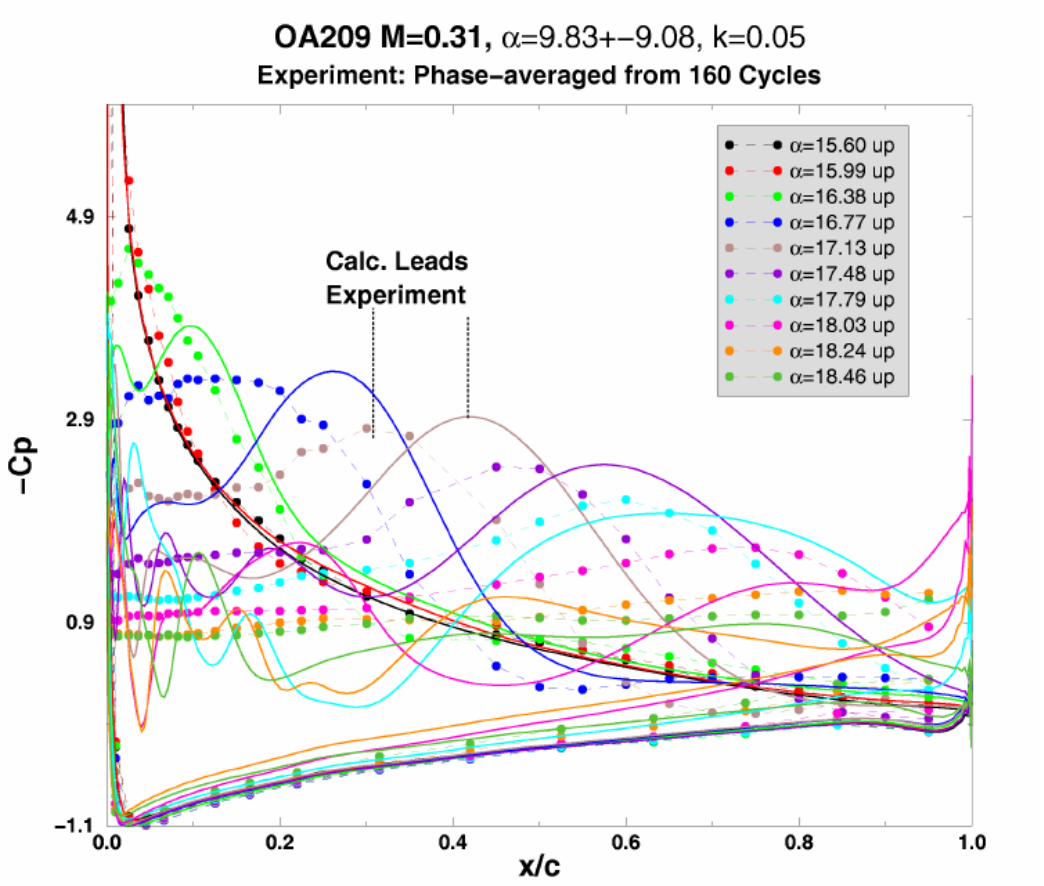

Fig.11: Chord-wise pressure distributions during the process of dynamic stall onset and beyond. Deep dynamic stall case of Figs.6 and 7.

5.4 PIV results

With the PIV test set-up described in section 4 the details of the instantaneous flow fields can be studied and also compared with the calculated data. Of some importance is the distribution of vorticity above the airfoil although vorticity must be calculated by differentiation of measured velocities. This procedure always causes some scatter in the results as can be observed from the following figures.

Figs. 12 display a sequence of instantaneous vorticity distributions during a deep dynamic stall cycle (for parameter details see Figs.6 and 7).
The left figures show results from the PIV recordings; the right figures show corresponding numerical data. In both experiment and calculation the definition of dimensionless vorticity is the same, the colour bars show equal ranges.
As was expected the experimental data show some scatter also in the outer flow regimes due to the calculation process from velocity to vorticity incorporating numerical differentiation. The calculation is of course free from scatter.

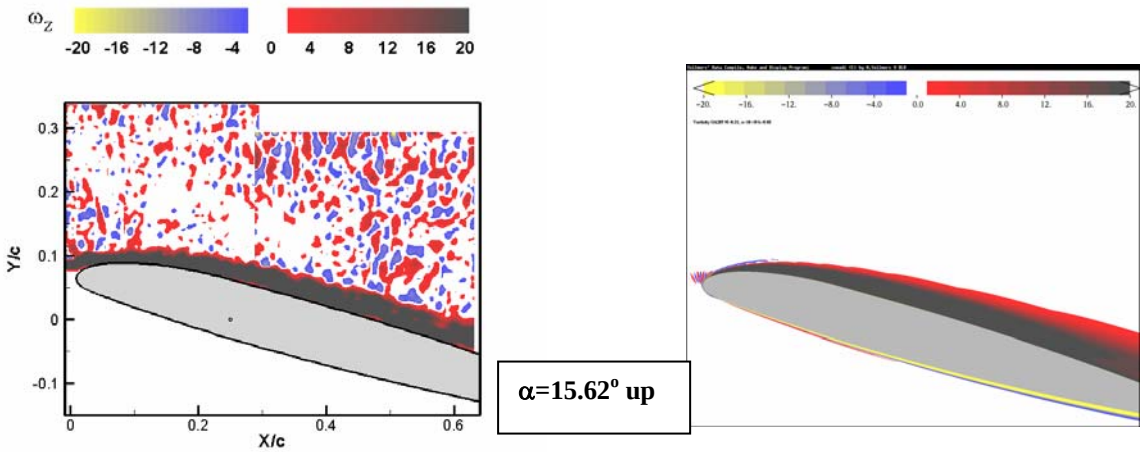

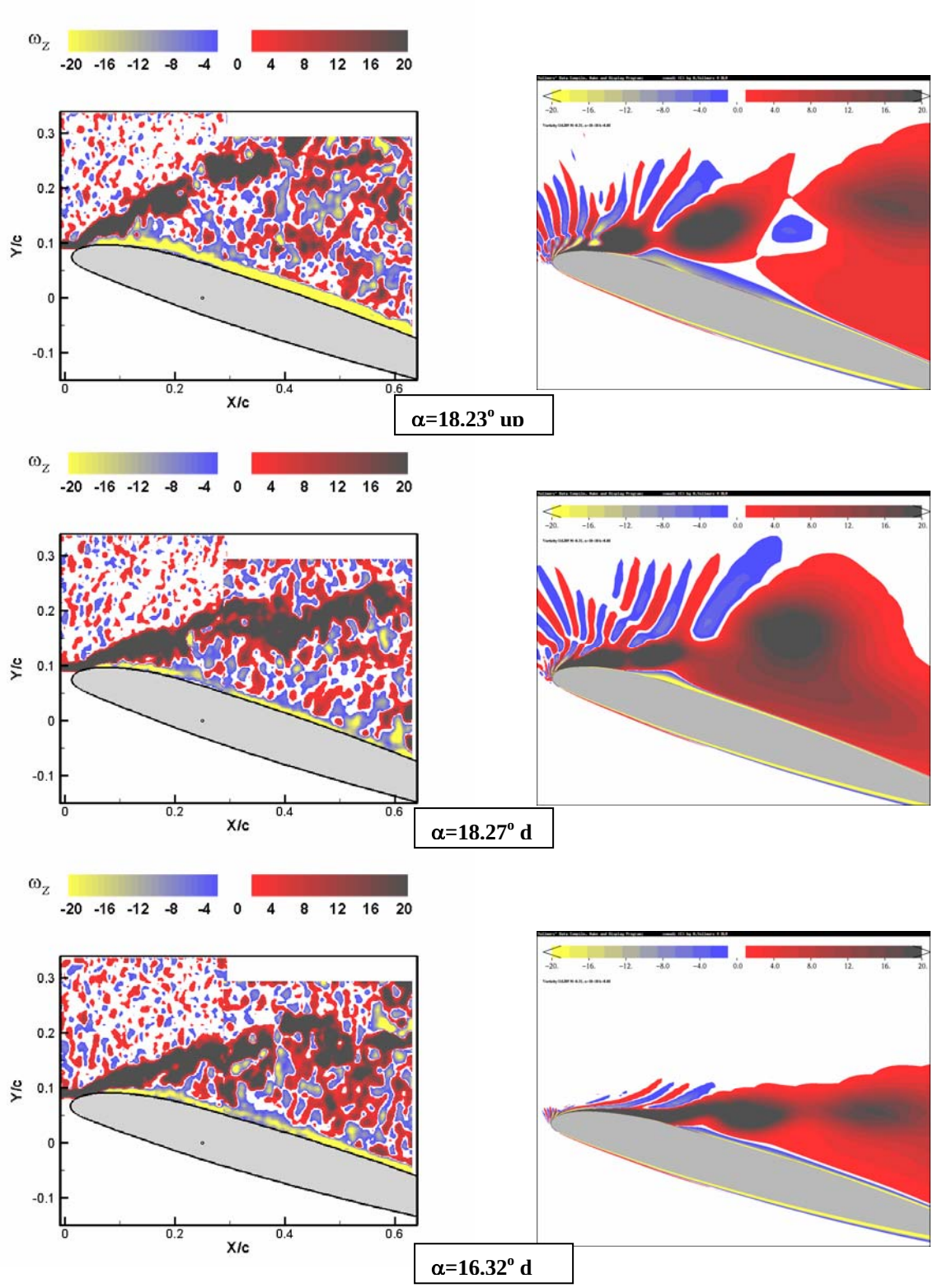

Fig.12: Measured vorticity distributions **Calculated vorticity distributions.**

The sequences of figures 12 show that dynamic-stall onset occurs beyond α=15.6° up-stroke, at α=18.23° up-stroke the dynamic-stall vortex is already moving out of the displayed frame which is in correspondence with the chord-wise pressure distributions of Fig.11. At α=18.27° down-stroke a secondary strong vortex is created and moves down stream until the last pair of figures shows the start of reattachment of the flow from the leading edge. In coincidence with Fig.6a the reattachment process starts earlier in the cycle for the calculation compared to experiment which is also seen in the last PIV vorticity field where severe separation is still existent (α=16.32° down-stroke).

6. Wing with Vortex Generators.

During the final part of the wind-tunnel tests on the OA209 airfoil model first investigations of **L**eading **E**dge **VO**rtex **G**enerators called LEVOGs have been carried out. From the knowledge base acquired at numerous wind-tunnel tests and numerical calculations this way to sufficiently and successfully influence dynamic stall is straightforward. It is obvious that the dynamic stall vortex development, movement and shedding plays a key role in this respect. The amount of vorticity included in this concentrated vortex is created mainly close to the leading edge during the up-stroke motion. A reduction of vorticity development is therefore necessary to improve dynamic stall characteristics.
Figs.13 shows the investigated devices: They are of cylindrical shape and have been arranged close to the airfoil leading edge: symmetric to the line z=0 (upper figure) and at a small distance shifted towards the lower airfoil surface with s as the distance of the generator's side-edge from z=0 (lower figure).
A number of devices with different diameters d and heights h have been investigated. Best results have been achieved with the devices sketched in

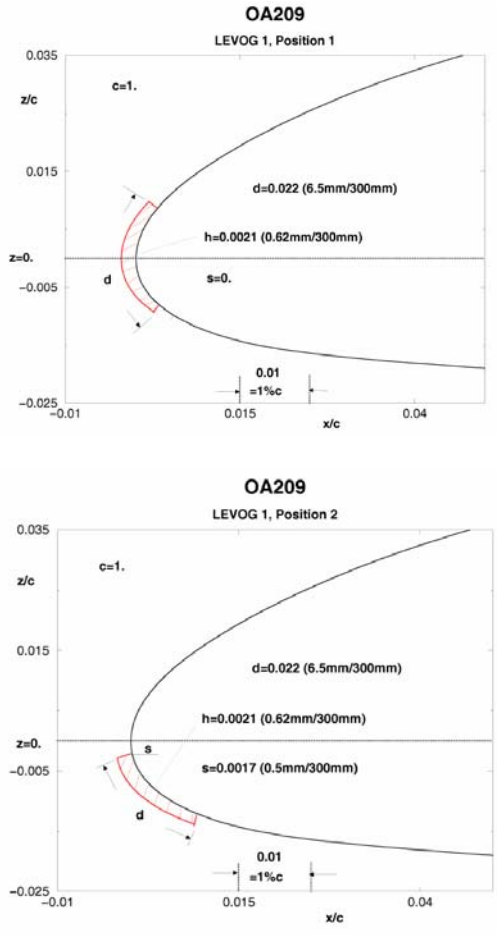

FIG:13: Locations and dimensions of investigated LEVOGs

Fig.13: h/c=0.0021, d/c=0.022 (c=airfoil chord).
Some of the results achieved for both light and deep dynamic-stall cases will be presented for the two positions: s/c=0 and s/c=0.0017.

6.1 Force- and Moment Hysteresis Loops.

The following experimental results have been measured at the same position (at mid-span) as the results discussed for the clean wing configuration. The span-wise distribution of LEVOGs plays an important role for their optimal efficiency. In the present case a span-wise distance of 0.047 referred to chord has been realized and is assumed as a rather dense arrangement. The span-wise generator distribution has been arranged such that the mid-span is located in the middle between two devices.

- **Deep Dynamic Stall**

Fig.14 shows lift-, pressure-drag- and pitching moment hysteresis loops for the deep dynamic stall case:

α=12.9+/-7.1^o, M=0.31, Re=1.15x10^6, k=0.05

which differs slightly from the case discussed previously. The plots include the two cases:

1) clean wing (red curves)
2) with LEVOGs (black curves)

In **Fig.14a** the devices have been arranged symmetrical to the airfoil leading edge at z=0 (see Fig.13 upper, s/c=0). The figures include the changes of force- and moment peaks w/o device: The maximum lift in the present case is reduced by 8.4% the maximum drag and minimum moment peaks however have been reduced with the device by as much as 24.7% and 32.6% respectively.
These changes due to the LEVOGs are quite remarkable as far as drag and moment is concerned. However the reduction of maximum lift is not desirable at all.
Shifting the devices slightly towards the airfoil lower surface as indicated in Fig.13 lower with s/c=0.0017 leads to the plots of **Fig.14b**. Now we have a reduction of drag and moment peaks of 19.1% and 31.3% respectively but the maximum lift stays almost unchanged.
These results are very surprising insofar as the only difference between Figs.14a and 14b is a rather small shift of the LEVOGs towards the lower airfoil surface all other parameters remained unchanged. Some other locations have also been tried but did not show improvements. Also the change of the device height and/or diameter did not show improvements either.
So the optimum effect has been derived with the parameter set of Fig.14b. However time was too short during the present tests to more systematically

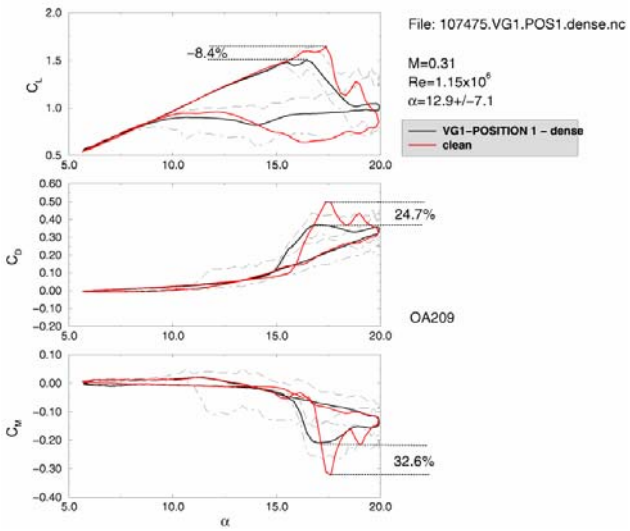

Fig.14a: Lift-, pressure-drag- and moment loops with LEVOGs at position 1 (s/c=0); Deep dynamic stall

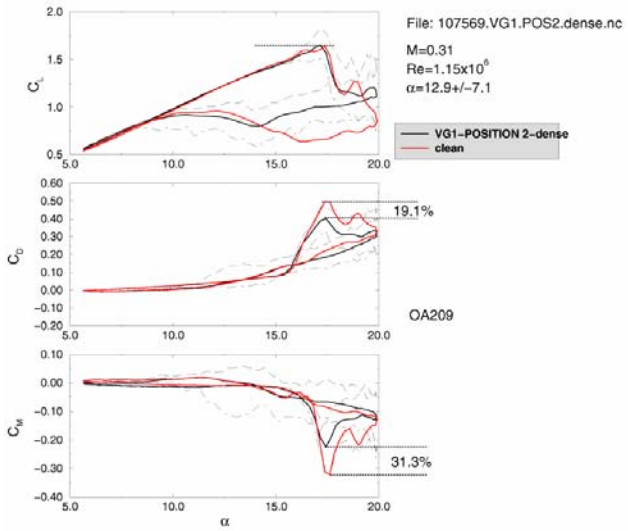

Fig.14b: Lift-, pressure-drag- and moment loops with LEVOG's at position 2 (s/c=0.0017); Deep dyn. stall

change parameters. This has to be done in a second tunnel entry to be scheduled for mid-2005. Then the variation of the span wise distance of devices and their location with respect to the mid-span pressure and PIV measuring section has to be varied as well.

- **Light Dynamic Stall.**

Figs. 15a and b show the corresponding results for the light dynamic stall case of Figs.8 and 9. The parameters concerning the LEVOGs dimensions and their chord-wise and span-wise positions are exactly the same as in the previous deep dynamic stall case, Figs13 and Figs.14.
For s/c=0, Fig.15a, an undesirable strong increase of moment and in particular drag peaks (more than 50%) has been achieved by the application of the devices compared to clean wing.

The maximum lift in this case remains almost unchanged.
Changing the position of the devices to s/c=0.0017, Fig.15b, the effects are completely different, i.e. improved: The maximum lift remains unchanged again, but the maximum drag is reduced by 22% and the minimum pitching moment is reduced by as much as 41%.
Due to the efficiency of the LEVOGs and the importance of their dimensions but in particular their location on the airfoil surface a patent has been applied for, [18].
In addition to these improvements it has to be checked of whether the devices have negative influences on the lift- and drag polars in the low incidence regime.

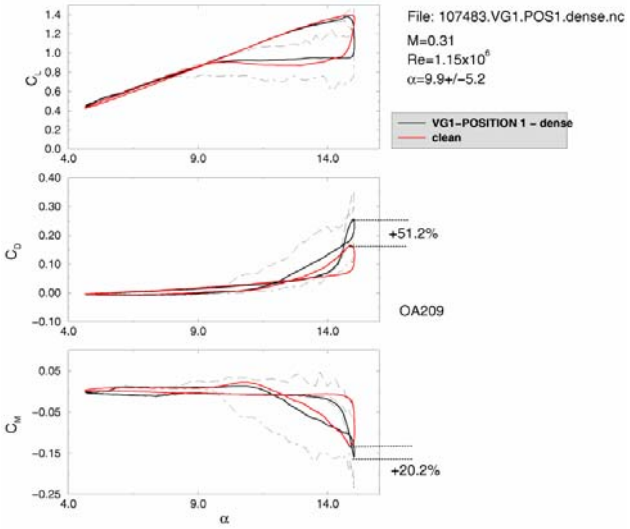

Fig.15a: Lift-, pressure-drag- and moment loops with LEVOGs at position 1 (s/c=0); Light dynamic stall

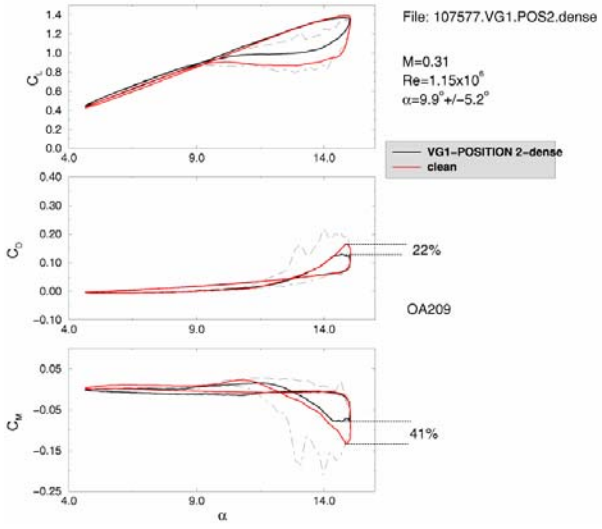

Fig.15b: Lift-, pressure-drag- and moment loops with LEVOGs at position 2 (s/c=0.0017); Light dyn. stall

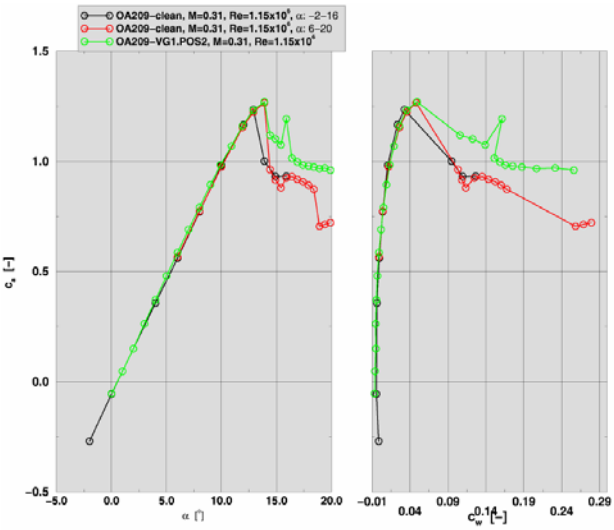

Fig.16: Lift- and pressure-drag polars w/o LEVOGs

Fig.16 shows lift- and pressure-drag polars for the flow cases :

1) clean wing
2) with LEVOGs with their optimum size and arrangement (see lower Fig.13).

In the lower incidence regime almost no lift variation and definitely no pressure-drag increase can be observed. However beyond c_{lmax} the lift stays at a higher level compared to the clean wing case which means an improvement here.
At higher Mach numbers up to transonic flow negative effects of the devices are also missing (not displayed here).

6.2 Flow field investigations with PIV.

For all measurement points and also for the test points measured with LEVOGs, PIV recordings have been taken in the mid-section in addition to unsteady pressure distributions. **Figs.17** show a sequence of vorticity distributions from PIV recordings at deep dynamic stall of Figs.14.

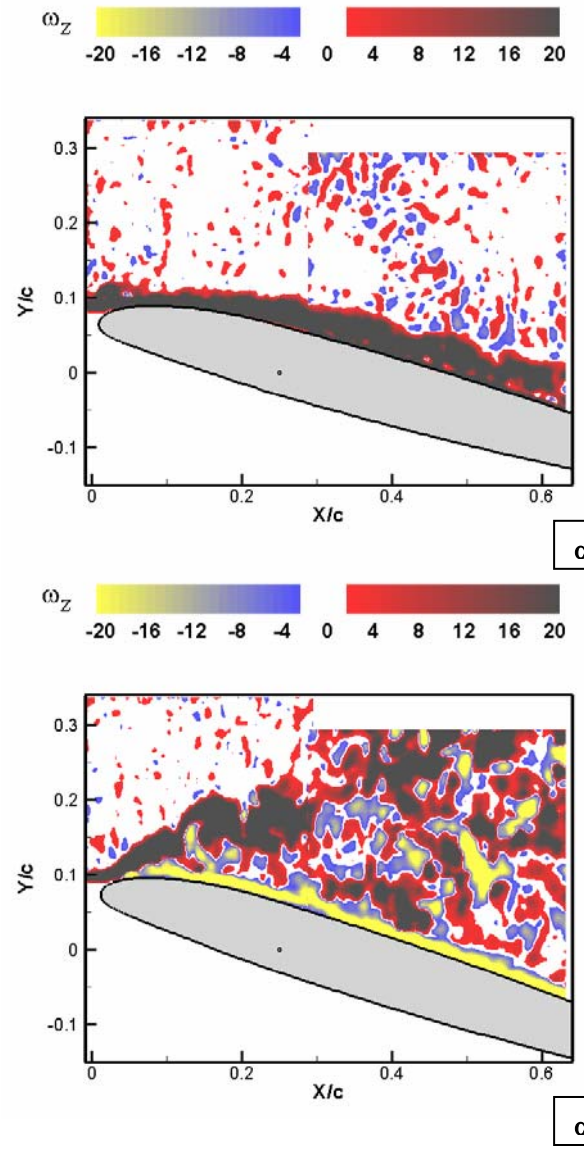

Fig.17a: Vorticity distributions from PIV-recordings; Clean wing

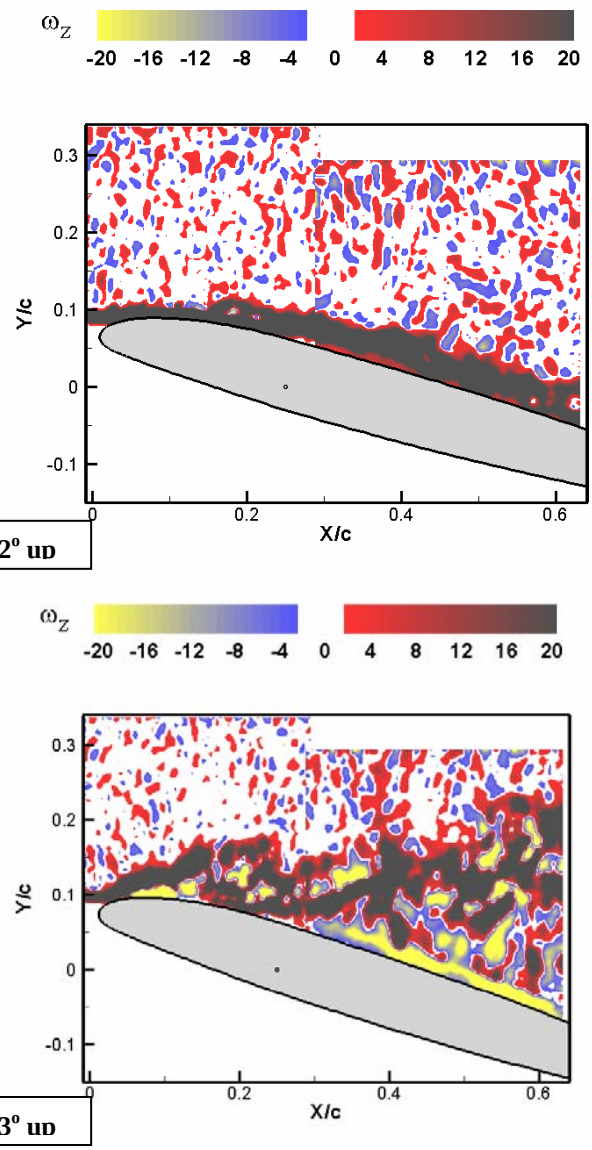

Fig.17b: Vorticity distributions from PIV-recordings; Optimum LEVOGs

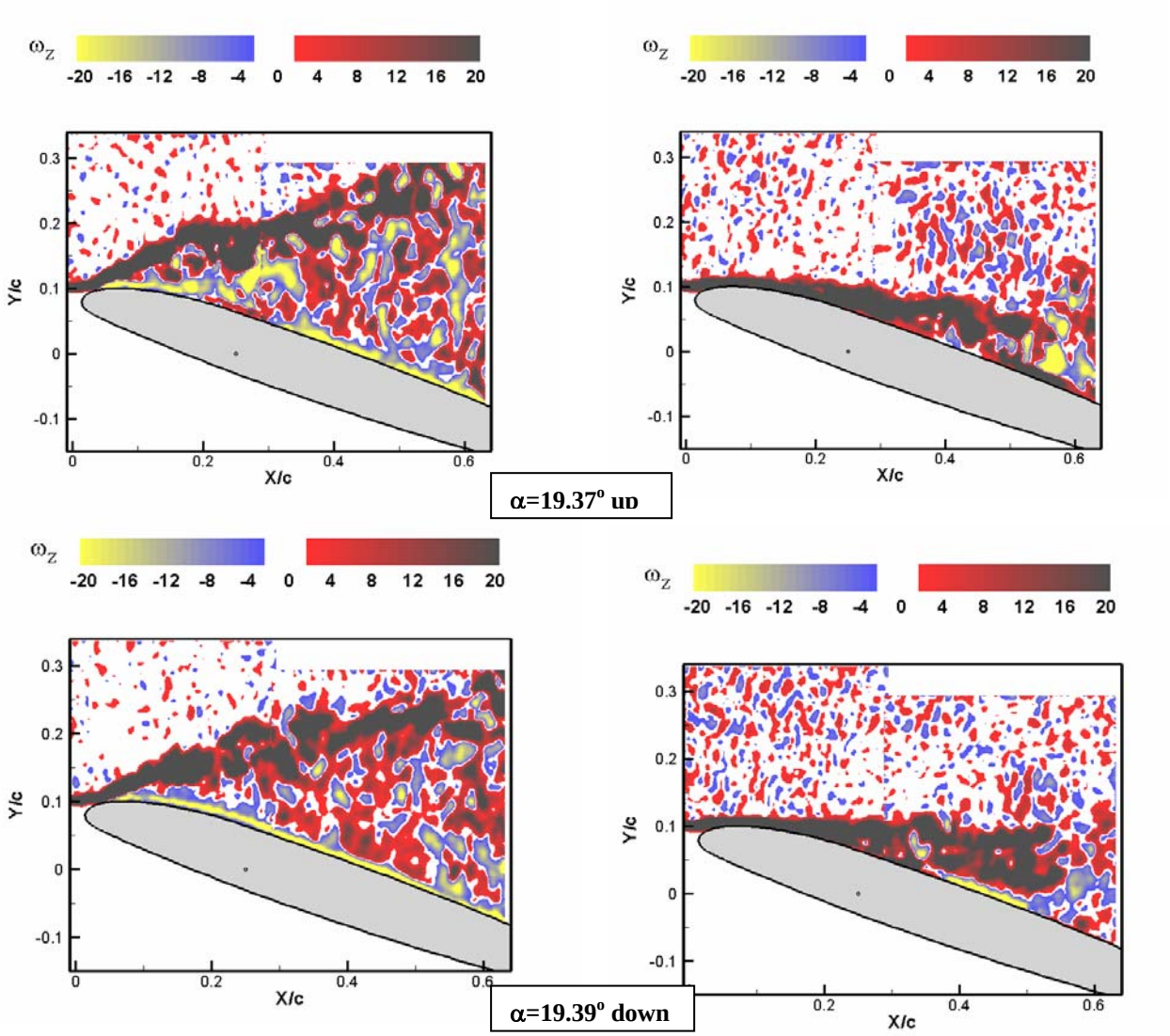

The left-hand sequences of Fig.17 display the clean wing case, the right hand sequences show vorticity distributions with the optimum size and arrangement of LEVOGs as indicated in Fig.13, lower.

Up to α=15.62° up-stroke no differences between clean wing and LEVOGs cases are detected. At least up to this incidence the flow is attached. About 2° later at α=17.83° up-stroke some remarkable differences are visible: The clean wing distribution shows almost complete separation from the leading edge, with LEVOGs present, vorticity shedding takes also place, but the vorticity layer is kept much closer to the wing upper surface. This behaviour is even more pronounced at α=19.37° up-stroke: Now the vorticity layer of the LEVOGs-case is kept very close to the surface similar to a boundary layer. Separation is almost avoided at this time-instant.

Also at the beginning of the down-stroke the differences are severe. Strong separation effects and vorticity spreading is almost avoided. Looking through all sequences measured it also happened that within small time-instants the flow with LEVOGs included shows stronger separation effects but short time later the flow reattaches. A kind of fluctuation took place during the high incidence part of the cycle. These effects have to be investigated more in detail in future tests.

Concerning the reasons of the favourable influences of the LEVOGs on dynamic stall characteristics it is assumed that the devices them self develop small and local vortices which start to interact with the developing dynamic stall vortex. How this interaction works and why the LEVOGs-position on the airfoil plays such a dominant role has to be studied in future investigations. In this respect the numerical investigation of the flow details at and in the vicinity of the devices may clear the situation considerably. DLR is planning to do these calculations on the basis of a 3D-unsteady NS-Code, the DLR-TAU-Code.

7. Conclusion, Future Activities.

Numerical and experimental investigations of dynamic stall on the OA209 airfoil section have been carried out within the scope of the DLR-ONERA joint project "Dynamic Stall". For the clean-wing configuration force- and pitching-moment hysteresis loops have been shown for both light and deep-dynamic stall cases. The experimental data have been compared with numerical results. In general it can be stated that quite good correspondences exist in most of the flow cases investigated. This holds also for regions of primary and secondary vortex development, movement and shedding and severe separation. It was pointed out, that the measured curves show considerable scatter which must be attributed to turbulence activities of the oncoming flow. These effects can not be simulated with existing RANS-codes. It was also shown that laminar-turbulent boundary-layer transition plays an important role and has to be taken into account in the calculations.
The second part of the present investigation was concentrated on passive control devices by means of miniature vortex generators (LEVOGs). The special devices investigated in the present wind-tunnel campaign have developed their efficiency on dynamic-stall characteristics at very special locations on the airfoil surface. Surprising improvements have already been achieved during these tests. However the amount of parameters to be investigated is excessive. Numerical 3D-calculations resolving the flow details in the vicinity of the devices should be very helpful to understand the obtained improvements. These calculations should be guided by corresponding experiments. For the LEVOGs a patent has been applied recently.

References.

[1] McCroskey,W.J.,"Unsteady Airfoils", Ann. Rev. Fluid Mech.,Vol.14, Pages 285-311,1982.

[2] Carr,L.W.,"Progress in Analysis and Prediction of Dynamic Stall", AIAA Atmospheric Flight Mech. Conf., Snowmass, Co.,Aug.19-21,1985.

[3] Carr,L.W.,Chandrasekhara,M.S., "Compressibility Effects on Dynamic Stall", Prog. Aerospace Sci., Vol.32, pp.523-573,1996.

[4] Geissler,W.,Carr,L.W., Chandrasekhara,M.S.,Wilder,M.C. ,Sobieczky,H., "Compressible Dynamic Stall Calculations Incorporating Transition Modelling for Variable Geometry Airfoils", 36th Aerospace Sciences Meeting & Exhibit, Jan.12-15,1998,Reno NV.

[5] Geissler,W.,Dietz,G.,Mai,H.,"Dynamic Stall on a Supercritical Airfoil",29th European Rotorcraft Forum,Friedrichshafen, Germany, 16- 18 Sept.2003.

[6] Geissler,W.,Dietz,G.,Mai,H.,Junker,B., Lorkowski,T., "Dynamic Stall Control Investigations on a Full Size Chord Blade Section", 30th European Rotorcraft Forum,Marseille, France, 14-16. Sept. 2004.

[7] MartinP.B.,McAlister,K.W., Chandrasekhara,M.S.,Geissler,W., "Dynamic Stall Measurements and Computations for a VR-12 Airfoil with a Variable Droop Leading Edge", 59th AHS-Annual Forum, Phoenix,Az, May 6-8,2003.

[8] Carr,L.W.,Chandrasekhara,M.S.,Wilder,M.C., Noonan,K.W. "The Effect of Compressibility on Suppression of Dynamic Stall Using a Slotted Airfoil",36th Aerospace Sciences Meeting & Exhibit, Jan. 12-15,1998,Reno,NV.

[9] Geissler,W.,Trenker,M.,Sobieczky,H.,"Active Dynamic Flow Control Studies on Rotor Blades", Research and Technology Agency, Spring 2000 Symposium on Active Control Technology, Braunschweig,Germany,8-12 May,2000.

[10] Geissler,W.,Sobieczky,H.,Trenker,M., "New Rotor Airfoil Design Procedure for Unsteady Flow Control",26th European Rotorcraft Forum, The Hague, The Netherlands, Sept.26-29,2000.

[11] Geissler,W.,Trenker,M.,"Numerical Investigations of Dynamic Stall Control by a Nose-Drooping Device", AHS-Aerodynamics, Aeroacoustics and Test Evaluation Technical Specialist Meeting, San Francisco,CA,Jan.23-25,2002.

[12] Geissler,W.,"Instationäres Navier-Stokes Verfahren für beschleunigt bewegte Profile mit Ablösung (Unsteady Navier Stokes Code for Accelerated Moving Airfoils Including Separation)", DLR-FB 92-03 (1993).

[13] Beam,R.M.,Warming,R.F.,"An Implicit Factored Scheme for the Compressible Navier-Stokes Equations", AIAA-J, Vol.16,No.4,April, 1978.

[14] Spalart,P.R.,Allmaras,S.R.,"A One-Equation Turbulence Model for Aerodynamic Flows",AIAA-paper 92-0439,January 1992.

[15]Geissler,W.,Chandrasekhara,M.S.,Platzer,M., Carr,L.W.,"The Effect of Transition Modelling on the prediction of Compressible Deep Dynamic Stall", 7th Asian Congress of Fluid Mechanics, Dec.8-12,1997,Chennai (Madras),India.

[16] Chen,K.K.,Thyson,N.A.,"Extension of Emmon's Spot Theory to Flow on Blunt Bodies", AIAA J.,Vol.9,1971,pp.821-825.

[17] Michel,R,,"Etude de la Transition sur les Profil d'Aile, Etablissement d'un Profile Incompressible", ONERA Dept.1/1578A(1951).

[18] Dietz,G.,Geissler,W.,Mai,H.,"Auftriebsfläche mit verbessertem Ablöseverhalten bei stark veränderlichem Anstellwinkel", Deutsche Patentanmeldung: DE 10 2005 018 427.8 (2005).